scientific reports

Insights from core/shell ZnCuInS/ZnS nanocrystals, type-II confinement, and implications for the design of safer industrial nanocrystals

Michał Zieliński[1,2]✉ & **Agnieszka Gajewicz-Skretna**[2]✉

In this study, we used an atomistic empirical tight-binding approach to systematically investigate the structural, electronic, and optical properties of cadmium-free ZnCuInS/ZnS core/shell nanocrystals over a wide range of core sizes, shell thicknesses, and core compositions. Starting with binary core systems (pure InS and CuS), we extended our analysis to alloyed cores, including $Zn_{1-x}In_xS$ and $Zn_{1-x}Cu_xS$, and to ternary ZnCuInS cores with varying copper (Cu)/indium (In) ratios. Our results showed that these nanostructures exhibited rich and diverse physical behaviors strongly dependent on composition and geometry. The introduction of In and Cu into ZnCuInS cores allowed for compositional tuning, providing control over key properties such as band gap energy, optical transition strength, and exciton-exciton interactions. To address the limitations of traditional confinement classification schemes, we introduced a set of complementary ways that quantify electron–hole overlap and spatial separation. These approaches provide deeper insight into the nature of exciton localization and facilitate the rational design of nanocrystals with tailored optoelectronic properties. Overall, our study demonstrates that atomistic modeling of ZnCuInS/ZnS nanocrystals provides a powerful method to engineer quantum dot performance through compositional and geometric optimization, paving the way for advanced applications in photonics, optoelectronics, and nanosafety.

Keywords Quantum dots, Core/shell nanocrystals, ZnCuInS/ZnS, Atomistic empirical tight-binding method, Spectral properties, Electronic properties, Band gap energy

The development of cadmium-free[1–10] (nano)materials, including quantum dots (QDs), has gained significant momentum in recent years due to the well-documented toxicity of cadmium-based compounds. Although cadmium has traditionally been preferred for QD synthesis due to its excellent optical and electronic properties, its significant health and environmental risks have driven efforts to find safer alternatives, such as zinc- or indium-based systems. Among these, novel indium-based QDs (often doped with copper) have emerged as promising candidates for next-generation applications, including light-emitting diodes, photovoltaics, and biomedical imaging. Their growing appeal is further enhanced by the rapid expansion of the nanotechnology sector, which is expected to reach a multi-billion-dollar market value in the near future. Nevertheless, despite being promoted as safer substitutes, both zinc and indium raise environmental and health concerns. Zinc, though considerably less toxic than cadmium, is toxic to aquatic organisms, potentially disrupting entire ecosystems by affecting trophic dynamics and biodiversity. Indium, meanwhile, has shown a tendency to bioaccumulate and cause organ toxicity after repeated or prolonged exposure, raising important questions regarding its safety, particularly in occupational and environmental contexts. Given the widespread and rapidly growing use of these materials, there is a pressing need for a systematic evaluation of their potential hazards to effectively mitigate their associated risks. Both experimental and computational methods are used to address these concerns. Although experimental toxicity testing remains a fundamental component of safety assessment, it is often time-consuming, resource-intensive, and not easily scalable, especially given the accelerated pace of new materials development. In this context, computational methods, including predictive modeling and in silico simulations, serve as valuable and

[1]Institute of Physics, Faculty of Physics, Astronomy, and Informatics, Nicolaus Copernicus University, Toruń, Poland. [2]Laboratory of Environmental Chemoinformatics, Faculty of Chemistry, University of Gdansk, Gdansk, Poland. ✉email: mzielin@fizyka.umk.pl; agnieszka.gajewicz@ug.edu.pl

efficient complements to traditional testing. These approaches enable the rapid screening of toxicity profiles and support the rational design of safer and more sustainable materials, while reducing the reliance on extensive animal testing and laboratory-based studies. The growing reliance on such computational strategies underscores the importance of continued research into material-specific properties, especially electronic structures, which play a critical role in determining a material's optical behavior, physicochemical properties, and interactions with biological systems. Parameters such as the highest occupied molecular orbital (HOMO)-lowest unoccupied molecular orbital (LUMO) band gap, conduction and valence band energy levels, and the density of states play a critical role in determining a material's reactivity, stability, and potential to generate reactive oxygen species (ROS). For example, a narrower band gap can facilitate more efficient ROS generation under ultraviolet irradiation, thereby increasing oxidative stress in biological systems. In contrast, modification of the electronic structure, through strategies such as doping, surface passivation, or particle size modulation, can suppress ROS generation and improve biocompatibility. For example, doping QDs with elements such as copper or palladium can alter their electronic properties and mitigate the leaching of indium ions in indium-based QDs. Therefore, a comprehensive understanding of the electronic structure is essential for the rational design of QDs with tailored properties for specific applications while minimizing their potential toxicity.

With the rapid advancement of computational capabilities in recent years, methods based on density functional theory (DFT)[11] have become increasingly popular for calculating the spectral properties of nanocrystals. DFT has shown considerable reliability in predicting certain material properties, such as the band gap of ZnS nanocrystals. However, significant limitations arise when DFT is applied to bulk band structure calculations for materials such as InS or CuS[12]. In such cases, DFT often predicts unrealistically small or even vanishing band gaps, which is in stark disagreement with experimental observations. This well-documented discrepancy has been reported in numerous studies[13–16]. Even the use of more sophisticated approaches, such as hybrid functionals (e.g., HSE06) or DFT + U methods (e.g., PBE + U) often fail to resolve the persistent underestimation of band gap energies. These shortcomings underscore a fundamental limitation of conventional DFT-based methods: their inability to consistently reproduce experimentally observed electronic properties in certain classes of materials. Overcoming this challenge has become a key goal in computational materials science, as accurate band structure predictions are essential for understanding and engineering materials with tailored electronic and optical properties[7]. In this study, we introduced an alternative approach to this long-standing problem: the atomistic empirical tight-binding (ETB) method. Over the past several decades, ETB has proven to be a remarkably versatile and reliable tool for modeling a wide range of nanostructured systems[18–20]. Unlike DFT, which relies on first-principles calculations, ETB uses parameterized atomic interactions to calculate electronic properties. This enables more efficient and accurate modeling, particularly in systems where conventional DFT methods struggle, such as those with complex band structures. By leveraging the strengths of ETB, we aimed to establish a robust and computationally efficient framework for predicting electronic and optical properties in materials where standard DFT methods face significant limitations.

In this study, we use the ETB method to systematically investigate the structural and electronic properties of ternary ZnCuInS/ZnS core/shell nanocrystals over a range of sizes and compositions. Our analysis began with pure InS and CuS cores and proceeded to explore alloyed cores, specifically $Zn_{1-x}In_xS$ and $Zn_{1-x}Cu_xS$, which contain two constituent materials. Of particular interest were the indium-rich systems ($Zn_{1-x}In_xS$), which exhibit a significant valence band offset (VBO) at the core/shell interface, resulting in complex behavior such as mixed confinement properties. This behavior contrasts with the more conventional and predictable trends observed in copper-rich systems ($Zn_{1-x}Cu_xS$). Despite these differences, our results highlight the need for a unified theoretical framework that considers key factors, such as strain and alloying, with equal importance given to fully understanding the underlying physics of the material systems under study. Building on these findings, we extended our investigation to ternary ZnCuInS nanocrystals by systematically varying the relative concentrations of Cu and In. This approach allowed us to explore how compositional tuning influences key material properties. While certain properties, such as the HOMO–LUMO energy levels, can be reasonably approximated by simplified models, others, most notably optical activity and the biexciton binding energies, exhibit complex, non-monotonic trends that reflect the interplay of numerous competing effects. This underscores the importance of performing detailed, system-specific calculations to accurately capture variations in core radii, shell thickness, and relative indium and copper concentrations. Therefore, we investigated the potential of ternary ZnCuInS/ZnS core/shell nanostructures to facilitate the efficient spatial separation of electrons and holes between the core and the shell, a characteristic of the type-II localization regime[11]. In many cases, however, the confinement character of such heterostructures cannot be readily determined using conventional approaches. To overcome this limitation, we propose a set of complementary methods for quantifying electron–hole overlap and spatial separation. These techniques provide a deeper insight into confinement dynamics and enable the rational design of QDs with tailored optoelectronic properties through computational modeling.

Results and discussion

ZnInS/ZnS systems

Figure 1 provides a schematic illustration of the core/shell spherical nanocrystals investigated in this study, with *R* representing the core radius and *H* the ZnS shell thickness. The core material could be either pure (unalloyed) InS or CuS, as shown in the figure, or highly alloyed materials such as $Zn_{0.5}In_{0.5}S$, which will be discussed later in the text.

The shell was consistently assumed to be pure, unalloyed ZnS. The band alignment between materials such as InS and ZnS—specifically, the VBO and conduction band offset (CBO), as described in the Methods section—results in a relatively deep confining potential for holes (valence band states) and a shallow potential for electrons (conduction band states). The band alignment and, hence, the behavior of both electrons and holes, strongly depend on the chosen value of the VBO[22], as well as the chemical composition of the core, since

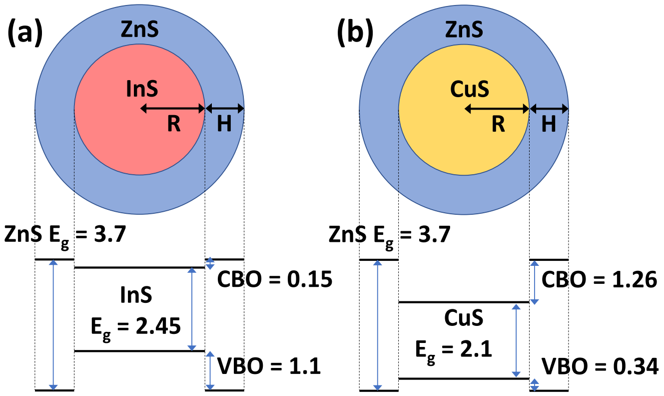

Fig. 1. Schematics of (**a**) InS/ZnS and (**b**) CuS/ZnS core/shell nanocrystals illustrating band gaps and band alignments. All values are presented in electron volts (eV). Note the very shallow potential well for electron states (0.15 eV) and the significant confinement of hole states (1.1 eV) in the InS/ZnS system.

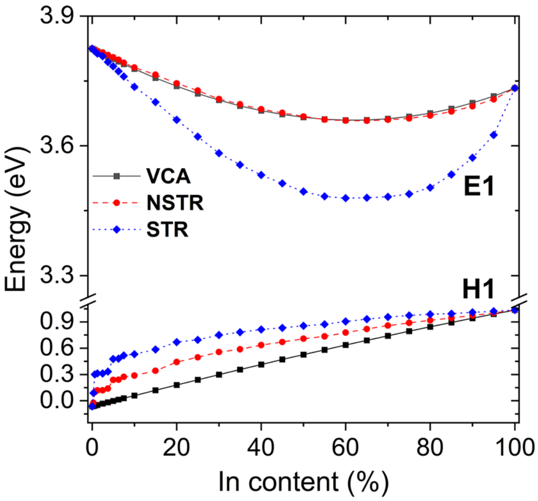

Fig. 2. Ground state electron (E1) and hole (H1) energy levels in 4.3 nm diameter $Zn_{1-x}In_xS$ nanocrystals plotted as a function of indium content (In%). Note the different energy scales used on the vertical axes and the pronounced bowing observed when both lattice randomness and strain (STR) are considered.

alloyed and unalloyed systems exhibit different band offsets. Despite the large ZnS band gap, a shallow electron confinement can lead to an enhanced leakage of electron states into the ZnS shell region, a phenomenon that will be discussed in detail in the following sections. In contrast, the band offset between CuS and ZnS provided effective confinement for both charge carriers. Therefore, type-II band alignment is not expected for this material combination, as discussed later in the text.

Level bowing due to intermixing

Nanocrystals are often highly alloyed and have mixed compositions. To understand the role of composition, we first studied a ‘core-only’ system ($Zn_{1-x}In_xS$ nanocrystals without a ZnS shell) with a diameter of approximately 4.3 nm (eight lattice constants). Figure 2 shows the evolution of the lowest electron (E1-LUMO) and hole (H1-HOMO) states as a function of indium (In) content analyzed at different levels of computational approximation. Within the virtual crystal approximation (VCA), the tight-binding parameters for the alloyed system were derived via linear interpolation between the bulk parameters of ZnS and InS. Despite the linear interpolation of the ETB parameters, the resulting energy evolution in the VCA can still exhibit non-linear behavior, as seen for the E1 state. This is because the band edges in tight-binding models non-linearly depend on the underlying ETB parameters[23]. To improve the VCA, we performed atomistic calculations that incorporated alloy randomness by randomly distributing individual In atoms throughout the lattice, though neglecting strain effects in this case (referred to as NSTR). In addition, we performed a full-scale atomistic calculation that incorporated alloy randomness and strain effects resulting from the lattice mismatch between InS and ZnS. While the VCA and NSTR results exhibited relatively small differences in electron energy levels, Fig. 2 clearly illustrates that the inclusion of strain effects becomes critical, especially in the intermediate composition range (i.e., strong alloying). Notably, even a low indium content (as low as 5%) led to a significant blue shift in the hole energy levels, accompanied by small spectral steps due to alloy-induced disorder.

Thus, the combination of alloying and strain induced significant bowing effects[24] for electrons and holes. As a result, a straightforward estimation of the optical spectra of alloyed $Zn_{1-x}In_xS$ nanocrystals, such as by the interpolation between pure ZnS ($x=0$) and pure InS ($x=1$) nanocrystals, can substantially overestimate the single-particle band gap, in some cases by as much as 0.5 eV. This result was obtained for nanocrystals without a shell. However, we also performed similar analyses for several core/shell structures with ZnS shells, which consistently confirmed the need to account for alloying effects at the atomistic level in all cases.

Valence band offset

Previously, we highlighted the effects of mixed composition. We further investigated the role of the InS/ZnS VBO and its effect on electron and hole wave functions, in particular their spatial localization. Figure 3 shows the radial probability densities of the ground-state electron (red) and hole (blue) wave functions (E1/H1) calculated for several selected VBO values in an InS/ZnS core/shell nanocrystal. The core radius and shell thickness were equal, each measuring 1.6 nm (corresponding to three lattice constants), resulting in an overall nanocrystal diameter of approximately 6.5 nm (12 lattice constants). The radial probability density represents the squared modulus of the wave function at a given distance from the nanocrystal center. Similar to the hydrogen atom, the wave function may peak at the center of the system. However, the radial probability density often reaches its maximum at some finite distance from the center. For example, in the case of the hydrogen 1 s ground state, the radial density peaks at the Bohr radius, even though the wave function itself peaks at the nucleus. This effect is illustrated in Fig. 3, where, for a VBO of 0.6 eV, the radial density of the E1 state exhibited a maximum at a certain distance from the center of the QD, with a pronounced tail extending into the shell region. In

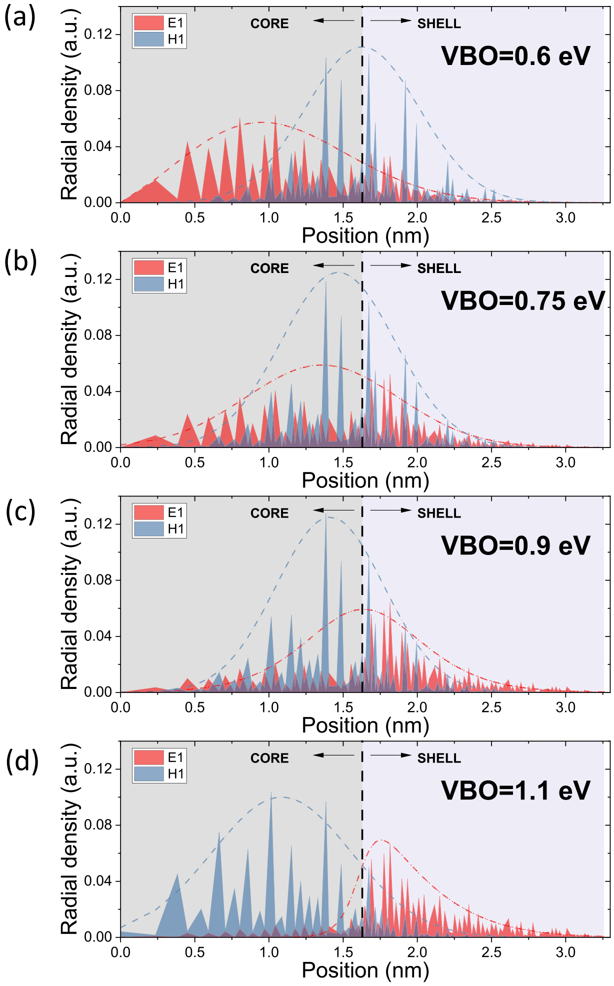

Fig. 3. Radial densities of ground state electrons (red) and holes (blue) as a function of the valence band shift for an InS/ZnS core/shell nanocrystal with R = H = 1.6 nm (corresponding to a total diameter of approximately 6.5 nm). For clarity, the core and shell regions are shown in different shades of gray (dark and light, respectively). The pronounced oscillations in the curves are due to the discrete nature of the atomic layers. The dashed lines surrounding the radial density curves are for visual guidance only.

contrast, the radial density of the H1 state peaked near the core/shell boundary, i.e., at the InS/ZnS material interface. By comparing the results obtained with and without strain effects (not shown here), we concluded that this unusual hole localization arose due to strain effects. When the strain effect was neglected, the radial density of the hole tended to be localized within the core region, similar to the electron state. As the VBO increased, two notable effects occurred. First, the radial density of the hole gradually migrated back toward the core region. This behavior is attributed to the deeper hole confinement potential induced by the increasing VBO, which favors core localization. In this sense, a larger VBO appears to partially counteract the strain-induced delocalization. Second, the electron was gradually pushed into the shell region. This shift resulted from a concomitant decrease in the CBO (Fig. 1), which facilitated electron leakage into the ZnS shell and led to dominant electron localization at higher VBO values. Consequently, the VBO plays a crucial role in shaping the spatial distribution of the electron and hole wavefunctions. At low VBO values, the system exhibits quasi-type-II confinement: the electron is mainly localized in the core, while the hole resides near the strained interface. For intermediate VBO values (around 0.75 eV), the radial density maxima of both carriers are aligned, resembling a typical type-I confinement. However, at higher VBOs, we observed type-II behavior (now more clearly defined) with the electron predominantly localized in the ZnS shell and the hole confined in the InS core. This type-II confinement pattern was particularly evident at the VBO value of 1.1 eV used in subsequent calculations, although we have also verified that this effect persists, and may even become more pronounced, at higher VBO values. In summary, the combination of significant strain and a large VBO at the InS/ZnS interface can induce a type-II confinement regime characterized by a remarkable spatial separation of the ground-state electron and hole radial densities.

Core size

In the previous section, we analyzed a core/shell nanocrystal with a fixed core radius and shell thickness, resulting in an overall diameter of 6.5 nm, as a function of VBO. From this point onward, we fixed the VBO for the InS/ZnS system at 1.1 eV (see Methods) and investigated nanocrystals with the same overall diameter (~6.5 nm), but with different core radii and corresponding shell thicknesses (i.e., maintaining R + H≈3.3 nm). As shown in Fig. 4, spatial separation of the electron and hole radial density maxima was observed for different core/shell configurations. The hole tended to localize within the core, with its density maximum occurring at approximately half the core radius. In contrast, the electron ground state was generally confined to the shell region, with its density maximum located near the core/shell interface, at a distance of approximately 0.2 nm. This effect was particularly pronounced in the case of a small core radius (R = 1.1 nm) and a thick shell (H = 2.2 nm), marked in red in the figure, where the electron was strongly localized in the shell while the hole remained confined to the core. Conversely, for a larger core radius (R = 2.7 nm) and a correspondingly thinner shell (H = 0.6 nm; marked in green), the electron and hole density maxima remained spatially separated. However, a noticeable leakage of the electron wavefunction from the thin shell into the core was observed, which could potentially enhance the electron–hole overlap. As such, subtle differences are difficult to discern in Fig. 4; an additional quantitative measure was needed to evaluate the degree of type-II confinement, which is discussed later in the text.

Alloying

Core/shell nanocrystals are often alloyed because it reduces the number of defects at the core/shell interface, a common problem in nanocrystal growth. In the case of the pure InS/ZnS nanocrystals discussed above, we observed features indicative of type-II band alignment resulting from shallow electron confinement. This, in turn, resulted from a large VBO and a small CBO. However, in more realistic systems, such as alloyed $Zn_{0.5}In_{0.5}S$/

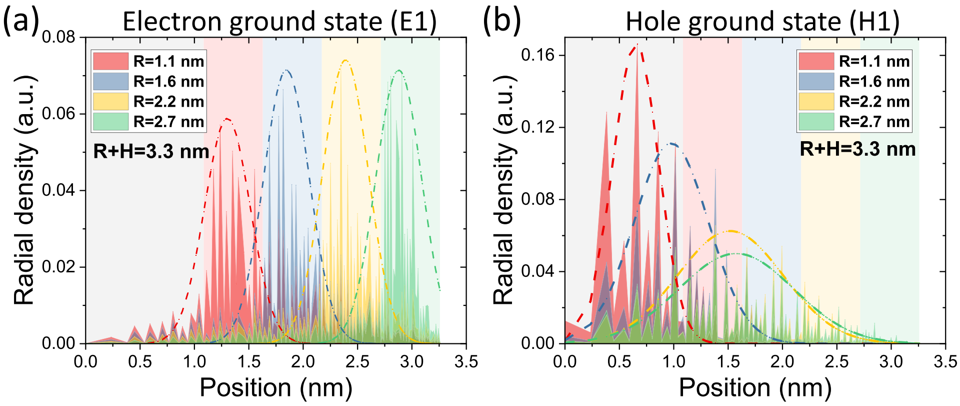

Fig. 4. Radial probability densities of ground state electrons and holes for four different InS core diameters (R = 1.1, 1.6, 2.2, and 2.7 nm), with the total nanocrystal radius fixed at 3.3 nm (corresponding to shell thicknesses (H) of 2.2, 1.6, 1.1, and 0.6 nm, respectively). The radial electron density is mainly localized in the shell region, although significant tails extend into the core. As the core diameter increases, the electron density shifts further away from the nanocrystal center. In contrast, the hole state remains predominantly localized in the core region. Different background colors are used to highlight variations in core/shell dimensions. Dashed lines are included for visual guidance only.

ZnS core/shell nanocrystals, one might expect this effect to be reduced, since the incorporation of ZnS into the core region significantly reduces the VBO, potentially suppressing type-II behavior. However, it is important to note that ZnS is a wide band gap material. Therefore, alloying the core with ZnS would also increase the 'effective' band gap of the core, potentially leading to a small CBO and reintroducing the possibility of type-II alignment. Previously, we emphasized the limitations of linear approximations in such systems due to strong bowing effects, so full electronic structure calculations are required to validate these hypotheses. As shown in Fig. 5, type-II-like confinement was observed in alloyed systems, especially for nanocrystals with a small core radius (R = 0.5 nm) and a relatively thick shell (H = 1.6 nm). As the core radius increased while the shell thickness remained constant, the system transitioned through an intermediate (mixed) regime and eventually reverted to conventional type-I confinement at R = 2.7 nm.

Core radius vs shell thickness

An analysis of radial density plots can be challenging due to the presence of long-tailed functions and pronounced oscillations between layers. For example, the electron and hole may localize on alternating layers, resulting in little overall spatial overlap despite similar envelope shapes. To better quantify the nature of the confinement, it is useful to introduce a numerical metric. Such an approach also allows for a systematic analysis over varying core radii (R) and shell thicknesses (H). To this end, Fig. 6 (top row) shows contour plots of the single-particle (HOMO–LUMO) band gap (i.e., $E_g = E1 - H1$) for a core/shell nanocrystal plotted as a function of R and H. Two systems are shown: a pure (InS/ZnS) structure (left column) and an alloyed ($Zn_{0.5}In_{0.5}S$/ZnS) structure (right column). In both cases, the emission energy was primarily controlled by the core radius, with the band gap decreasing significantly with increasing core radius. In contrast, dependence on the shell thickness was much weaker. While the overall trends were qualitatively similar between the pure and alloyed structures, the band gap in the alloyed case was typically larger by approximately 0.1–0.2 eV. At first glance, this increase in the band gap for the alloyed system may seem counterintuitive, especially in light of the substantial band gap bowing observed earlier for the x = 0.5 case without a shell (see Fig. 2). However, in the core/shell structures studied, which exhibited a large VBO, the hole state tended to localize in the indium-rich (core) region, i.e., in the center of the bowing plot in Fig. 2. In contrast, the electron preferred the zinc-rich (shell) region, i.e., toward the left side of the bowing curve. Consequently, for $Zn_{0.5}In_{0.5}S$/ZnS core/shell nanocrystals, the hole energy was lowered compared to the pure InS case, effectively increasing the band gap. Although the electron energy (E1) remained lower than in pure ZnS, it was still higher than in InS and ultimately contributed to the observed band gap increase in alloyed systems. This further emphasizes the importance of simultaneously considering multiple effects such as VBO, alloying, strain, and confinement. Notably, band gap energy (or emission wavelength) alone provides insufficient insight into the confinement character. One method of quantifying the electron–hole overlap (and, thus, confinement behavior) is to calculate the optical dipole moment of the interacting electron–hole pair (exciton), as described in the "Methods" section[11] This provides a measure of spatial overlap and confinement type (which will be discussed later). Accordingly, Fig. 6 (bottom row) plots the optical activity of the lowest excitonic state as a function of various core/shell dimensions for both the pure (left) and alloyed (right) systems. By systematically comparing the values from Fig. 6c,d over 40 different core/shell configurations (20 with and 20 without alloying) and correlating them with the corresponding radial density plots, we confirmed the emergence of a type-II confinement regime. This regime occurs predominantly in structures with small core radii and thick shells, in both pure and alloyed systems. Interestingly, alloyed systems tend to transition to type-II (or mixed) confinement more readily. However, caution should be exercised in interpreting optical activity results. For example, in the alloyed system with R = 2.7 nm and H = 1.1 nm (also discussed in Fig. 5c), the observed low optical activity arose from the localization of the electron and hole in different atomic layers rather than from large-scale spatial separation. In such cases, despite the reduced overlap, the confinement could still be classified as type-I.

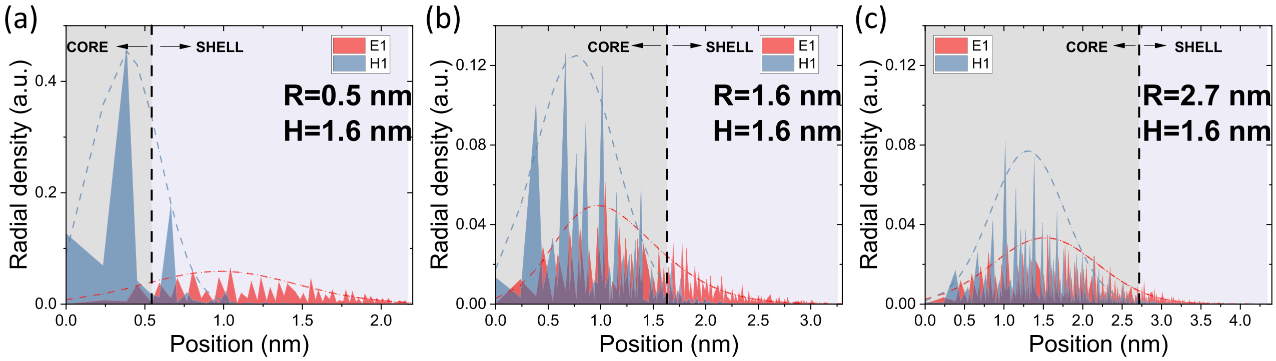

Fig. 5. Radial densities of ground-state electrons and holes for three different $Zn_{0.5}In_{0.5}S$ core diameters (R = 0.5, 1.6, and 2.7 nm, corresponding to 1, 3, and 5 lattice constants, respectively) with a constant ZnS shell thickness (H = 1.6 nm, or 3 lattice constants).

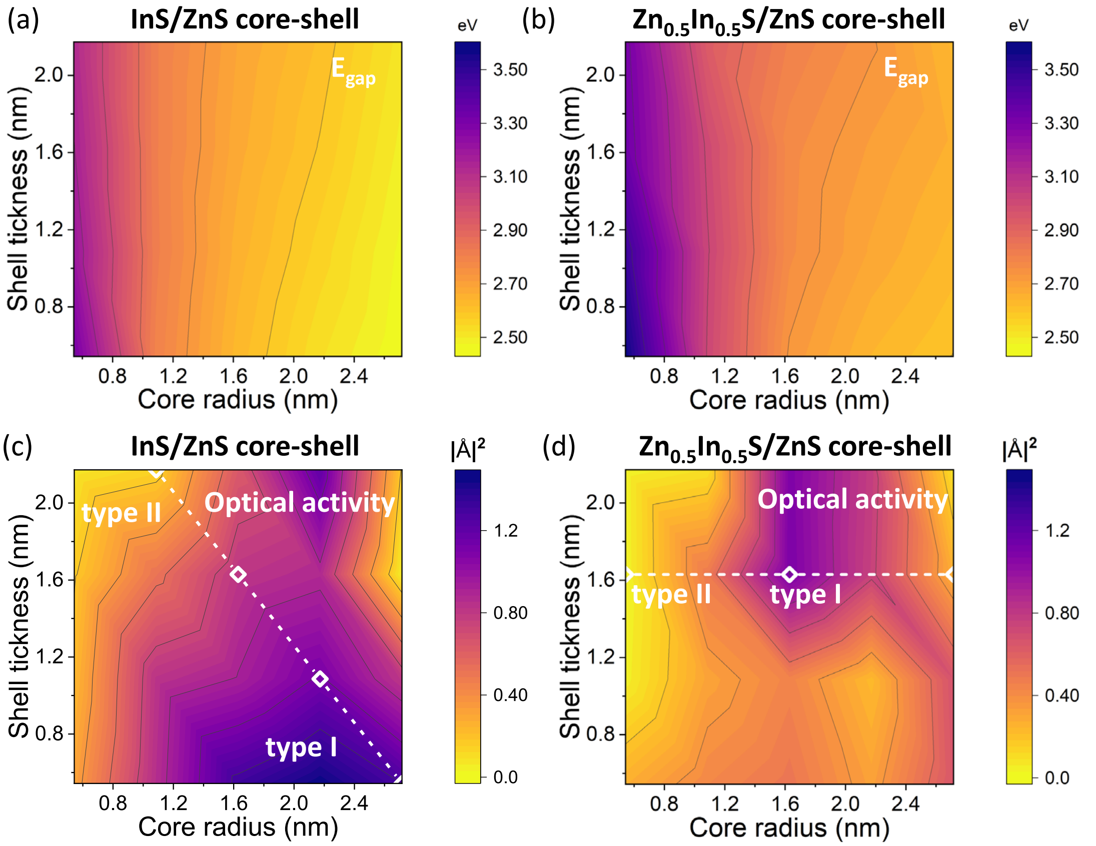

Fig. 6. (Top row) Single-particle band gap values (E_{gap} = E1-H1) as a function of core radius (R) and shell thickness (H). (Bottom row) Electron–hole transition dipole moments, as a measure of electron–hole spatial separation, plotted for different R/H ratios. The left column shows results for unalloyed InS/ZnS core/shell nanocrystals, while the right column corresponds to alloyed $ZnIn_{0.5}S$/ZnS systems. Small core radii combined with thick shells typically lead to increased electron–hole separation, indicating type-II confinement. White diamonds along the dashed lines indicate the specific R/H ratios for which radial density distributions are shown in Figs. 4 and 5.

ZnCuS/ZnS

In the following section, we repeated the calculations described above, this time replacing InS with CuS. For the sake of brevity, the discussion will focus primarily on the key differences between the two systems.

Level bowing due to intermixing

Figure 7 is analogous to Fig. 2, but shows results for the $Zn_{1-x}Cu_xS$ nanocrystal. Compared to the InS cases, the electron and hole states in $Zn_{1-x}Cu_xS$ exhibited a relatively minor bowing effect, with minimal differences observed among the three computational approaches used. Notably, the results obtained with and without strain inclusion were nearly indistinguishable. This can be attributed to the significantly smaller lattice mismatch between CuS and ZnS compared to that between InS and ZnS.

Valence band offset

The evolution of electron and hole radial density distributions in CuS/ZnS nanocrystals, computed over a range of relevant VBO values, is shown in Fig. 8. For all considered VBO scenarios, both electron and hole densities remained predominantly confined to the core region, with only small tails extending into the shell. As expected, increasing the VBO led to a stronger localization of the hole in the core. Although a slight inward shift of the hole density towards the center of the nanocrystal was observed, the overall confinement character remained type-I. Nevertheless, some spatial separation between the electron and hole envelope maxima was evident. Interestingly, the actual radial density maxima—not just the envelope centers—appeared to be located in different atomic layers for the electron (red) and hole (blue). This spatial mismatch could potentially reduce the electron–hole overlap and decrease the oscillator strength, even in nominally type-I confinement systems.

Core size and alloying

In the case of CuS/ZnS systems, both electron and hole states were consistently found to be strongly confined within the core region. As a result, a figure analogous to Fig. 4 has not been included. However, Fig. 9

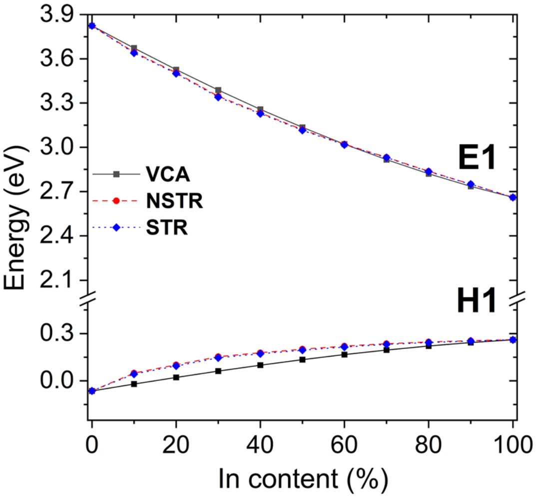

Fig. 7. Ground state electron (E1) and hole (H1) energy levels in 4.3 nm diameter $Zn_{1-x}Cu_xS$ nanocrystals plotted as a function of copper content (Cu%). Note the different energy scales used on the vertical axes and the pronounced bowing observed when lattice randomness and strain (STR) are considered.

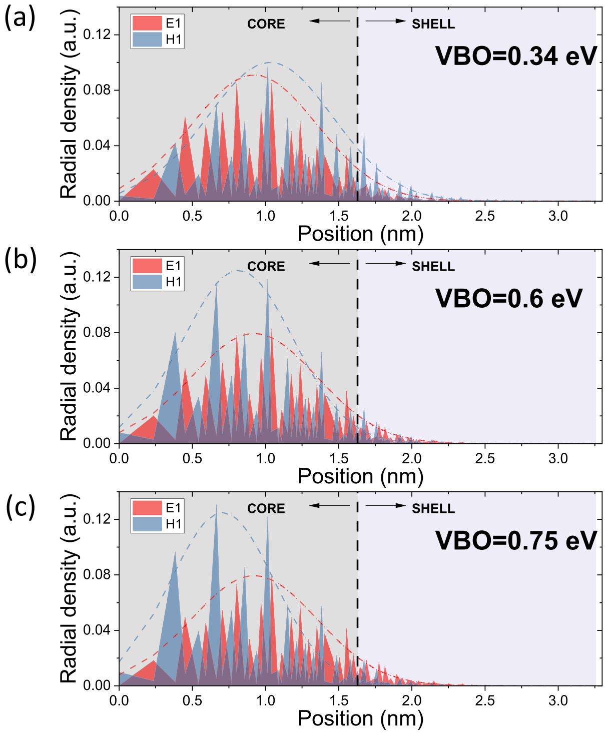

Fig. 8. Radial densities of ground state electrons (red) and holes (blue) as a function of valence band shift for a CuS/ZnS core/shell nanocrystal with R = H = 1.6 nm (corresponding to a total diameter of approximately 6.5 nm). For clarity, the core and shell regions are shown in different shades of gray (dark and light, respectively). The pronounced oscillations in the curves are due to the discrete nature of the atomic layers. Notably, the maxima of the electron and hole distributions often appear at different distances from the center of the nanocrystal. The dashed lines surrounding the radial density curves are for visual guidance only.

(corresponding to Fig. 5) shows the radial density distributions of the ground-state electron and hole for three different core diameters in an alloyed $Zn_{1-x}In_xS$ system with a fixed ZnS shell thickness. As previously observed, both carriers were predominantly localized in the core, clearly indicating type-I confinement. Notably, in the smallest nanocrystal (Fig. 9a), the spatial separation between the electron and hole radial density maxima, i.e., their localization at different radial distances from the nanocrystal center, was most pronounced.

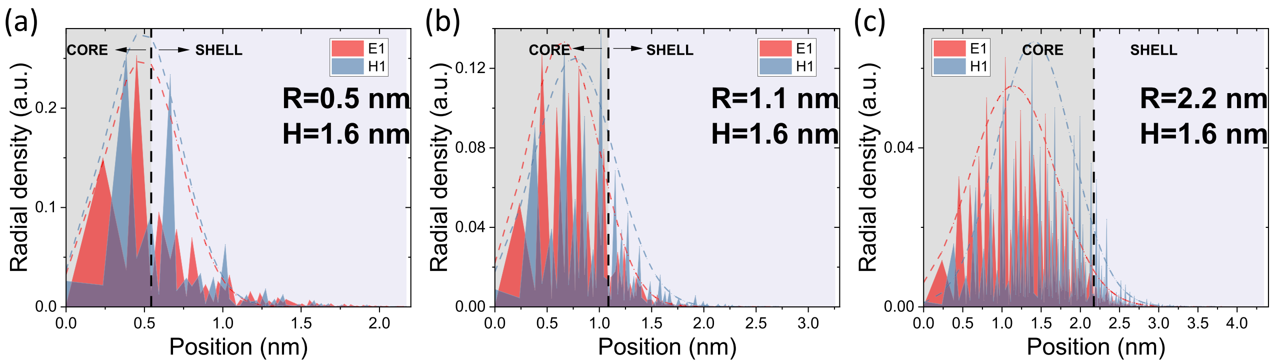

Fig. 9. Radial densities of ground-state electrons and holes for three different $Zn_{0.5}Cu_{0.5}S$ core diameters (R = 0.5, 1.6, and 2.7 nm, corresponding to 1, 3, and 5 lattice constants, respectively), with a constant ZnS shell thickness (H = 1.6 nm, or 3 lattice constants).

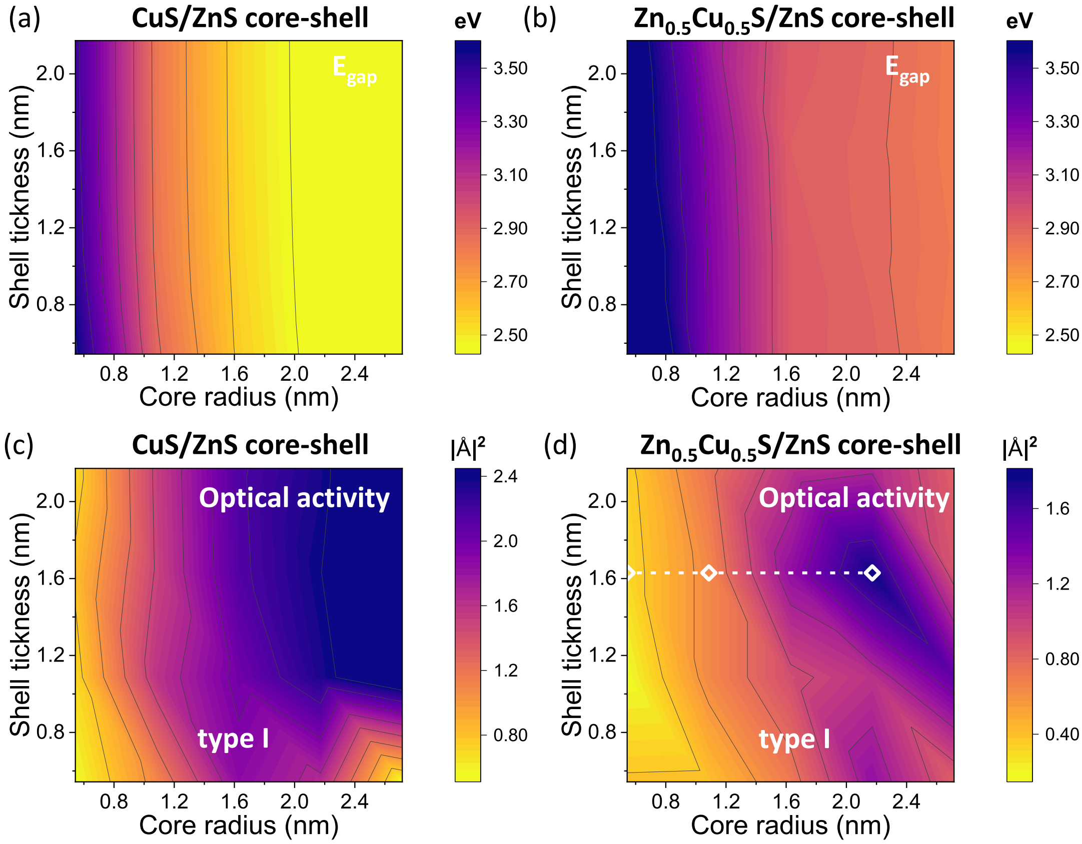

Fig. 10. (Top row) Single-particle band gap values (E_{gap} = E1-H1) as a function of core radius (R) and shell thickness (H). (Bottom row) Electron–hole transition dipole moments, as a measure of electron–hole spatial separation, are plotted for different R/H ratios. The left column shows results for unalloyed CuS/ZnS core/shell nanocrystals, while the right column corresponds to alloyed $Zn_{0.5}Cu_{0.5}S$/ZnS systems. Small core radii combined with thick shells typically lead to increased electron–hole separation, indicating type-II confinement. White diamonds along the dashed lines indicate the specific R/H ratios for which radial density distributions are shown in Fig. 9.

Core radius vs shell thickness

A systematic analysis of the electronic properties of CuS/ZnS and alloyed $Zn_{0.5}Cu_{0.5}S$/ZnS core/shell nanocrystals as a function of core radius and shell thickness is shown in Fig. 10. As expected, Fig. 10a,b show a characteristic decrease in the band gap with increasing core radius, reflecting a reduction in quantum confinement. In contrast, the band gap exhibited only a modest dependence on shell thickness, consistent with the limited spatial extension of electron and hole wavefunctions into the shell region. The most notable difference between the pure (i.e., unalloyed) and alloyed systems occurred in the band gap values: the alloyed nanocrystals exhibited a larger band gap, which was attributed to the presence of the wider band gap ZnS component within the core region of the alloyed nanocrystal. Interestingly, Fig.10c,d showed somewhat unusual behavior of the optical activity with increasing core radius. In the unalloyed system, except for very thin shells, the optical activity increased with core size. This trend can be attributed to the fact that the oscillator strength was linked to the electron–hole transition dipole moment, which, in turn, scales with the volume of the emitter. That is, larger nanocrystals tend to exhibit higher dipole transitions, and, in the case of CuS/ZnS QDs, this enhancement was not related to type-I or type-II confinement effects. As shown in Fig. 10c, the alloyed system exhibited a more complex pattern, likely due to the compositional randomness introduced by alloying. Nevertheless, all the analyzed alloyed structures remained within the type-I confinement regime, as confirmed by the radial density analyses presented in Fig. 9 (the three cases highlighted there are marked with white diamonds in Fig. 10c). In summary, a thorough analysis of both radial charge densities and optical activity is essential to reliably confirm or rule out the presence of type-II confinement.

Ternary ZnCuInS/ZnS core/shell nanocrystals

Thus far, we have focused on alloyed systems containing only two cations in the core, Zn and In or Zn and Cu. However, experimentally, both Cu and In can be co-alloyed with Zn to form a ZnCuInS core of variable stoichiometry, which can then be encapsulated in a ZnS shell. In the following section, we systematically investigated the properties of such ternary alloyed core/shell systems, with Cu and In concentrations ranging from 0 to 50%. The results are presented as two-dimensional contour plots showing variations as a function of Cu and In content, with the Zn concentration defined as Zn = 1−Cu−In. Since the binary systems $Zn_{1-x}In_xS$ and $Zn_{1-x}Cu_x$ have already been discussed over the full range of x, here we present our results using square plots (rather than the conventional triangular plots for ternary alloys), with Cu and In contents up to 50% each. To avoid confusion with previously presented results (e.g., those examining variations in core/shell sizes), we used a different color scheme. As it is not feasible to simultaneously plot the dependence on four parameters (Cu content, In content, core radius, and shell thickness) within a single plot, we limited the current analysis to a few, select core/shell size combinations. It should be noted, however, that only pure ZnS shells were considered in this study. Nevertheless, intentional or unintentional intermixing of the ZnS shell with core materials (InS or CuS) could be an interesting direction for future research.

Figure 11 shows the electron (E1), hole (H1), and excitonic ground state energies as a function of the indium and copper composition in the core. The E1 energy decreases largely in proportion to the incorporation of low band gap materials (CuS or InS) in the core region. Among these, CuS, which has the lowest band gap (2.1 eV), induces a slightly larger reduction in E1 compared to InS (2.45 eV), although both materials have a broadly similar effect on lowering the electron ground state energy. It is important to note, however, that this electron energy trend alone does not provide conclusive information about potential electron density leakage into the shell region, especially at higher In concentrations. In contrast, Fig. 11b shows that H1 energy is much more sensitive to increasing In content than to Cu content. This is mainly due to the much larger VBO between InS and ZnS (1.1 eV) compared to the smaller offset between CuS and ZnS (0.34 eV). The introduction of InS into the core (due to its large VBO) significantly increased the hole energy, making the In content the dominant factor shaping the H1 spectrum.

Figure 11c shows the excitonic band gap, which, unlike the single-particle gap (E1-H1), includes the effect of the electron–hole Coulomb interaction (see Methods). The excitonic ground state energy largely follows the trend of the E1 level, since the variations in the hole state due to alloying are comparatively smaller. The resulting excitonic energy, which corresponds to the photon emission energy from the lowest excitonic manifold, ranges from approximately 3.7 eV in nearly pure ZnS core/shell systems to 2.1 eV in systems with cores composed of a 1:1 In:Cu ratio (i.e., pure InCuS).

Since energy levels alone are relatively poor indicators of the spatial distribution of electrons and holes, in Fig. 12a-c we plotted the optical activity of three different nanocrystals as a function of composition, following

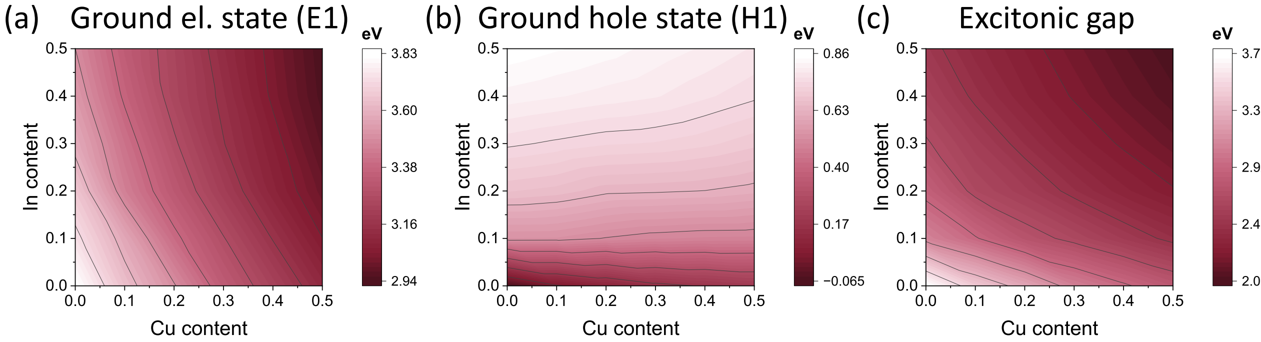

Fig. 11. Ground state energies of electrons (E1) and holes (H1), as well as the ground state exciton energy (corresponding to the excitonic gap), plotted as a function of Cu and In content in ZnCuInS/ZnS core/shell nanocrystals with a core diameter of R = 2.2 nm and a shell thickness of H = 1.1 nm.

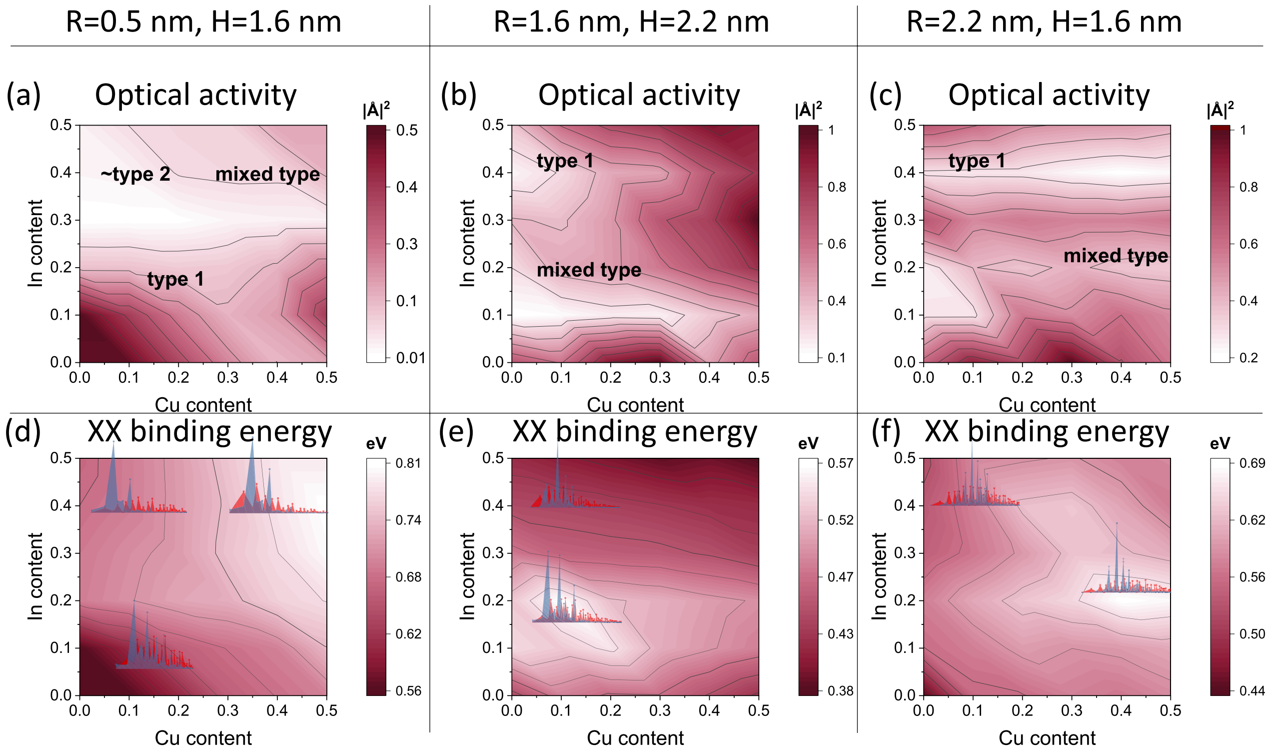

Fig. 12. (Top row) Optical activity, representing electron–hole overlap for three different ZnCuInS/ZnS core/shell nanocrystals; (bottom row) biexciton binding energy, serving as an indicator of electron–hole spatial separation, plotted as a function of Cu and In content. Note that each plot uses different units and scales.

the same approach as in the previous sections. In addition, the lower panels of Fig. 12d-f show the approximate biexciton (XX) binding energy, defined as $\Delta XX \approx J_{E1E1} + J_{H1H1} - 2J_{E1H1}$. This approximation was derived from three Coulomb integrals calculated for the electron and hole in their respective ground states, and neglects correlation and exchange effects[15]. Here, J_{E1E1} and J_{H1H1} represent the electron–electron and hole-hole repulsion, respectively, while J_{E1H1} corresponds to the electron–hole attraction. This ΔXX approximation serves as an additional metric to assess the spatial separation of the electron–hole. When considered together with the optical activity and radial density distributions, it provides valuable insight into the nature of the confinement regime of the nanostructures.

As shown in Fig. 12c, a clear type II-like confinement with pronounced electron–hole separation was observed only for nanocrystals with a small core radius (R = 0.5 nm) and a relatively thick shell (H = 1.6 nm), and only for compositions with high In and low Cu content (upper left corner of the plot). This conclusion is supported by the low optical activity and the relatively high biexciton binding energy (above 0.7 eV). However, the confinement was mixed or remained type-I for other compositions. For example, in nanocrystals with both high In and high Cu content (upper right region in Fig. 12a,d), we observed a substantial ΔXX and a low optical transition dipole moment. Nevertheless, the corresponding radial density plots showed a significant overlap between the electron and hole envelope functions. This suggests that low optical activity may result from localization of the electron and hole in different atomic layers, while a substantial ΔXX may result from shifted density maxima and different spatial distributions, without necessarily implying type-II confinement. Conversely, clear type-I confinement is observed in systems with low In and Cu contents. The remaining panels of Fig. 12b-c,e–f show nanocrystals with a constant total radius (R + H = 3.8 nm) but varying core/shell ratios. Although not shown here, we also confirmed that the composition-dependent trends for E1, H1, and exciton (X) energies were consistent with those shown in Fig. 11. It should be emphasized, however, that this consistency did not extend to optical activity or biexciton binding energy, both of which exhibited complex, non-trivial, and composition-specific behavior.

For example, in the upper left regions of Fig. 12b,f, we observed cases where low optical activity coincided with a large ΔXX, but the system remained in the type-I confinement regime. Both metrics suggest that the hole wavefunction was more spatially delocalized despite the type-I character. Similarly, in the lower left corners of Fig. 12b,e, a large ΔXX and low optical activity suggest significant shifts in the electron radial density maxima, but without a complete transition to type-II behavior. These cases can best be described as having 'mixed' confinement properties. A similar phenomenon was observed in the last system discussed here (R = 2.2 nm, H = 1.6 nm), especially for compositions with high Cu and intermediate In contents (Fig. 12c,f).

In summary, we conducted a thorough theoretical analysis of ZnCuInS/ZnS core/shell nanocrystals exhibiting different levels of alloying, shell thickness, and strain treatment. Our analysis revealed their rich and adjustable electronic and excitonic behavior, which is driven by compositional and structural variations. Through the combination of atomistic electronic structure calculations and excitonic and biexcitonic spectral simulations, we systematically examined the evolution of confinement regimes, including type-I, type-II, and a mixed regime. This process allowed us to uncover the underlying mechanisms that control state localization, dipole strength, and exciton-exciton interactions. Our results demonstrate that, even in structurally symmetric core/shell nanocrystals, atomic-scale effects and internal strain can lead to the partial or complete spatial separation of the electron and hole wavefunctions. This leads to a nontrivial dependence of the optical dipole moment and the biexciton binding energy (ΔXX) on composition and structural parameters, such as shell thickness. These metrics serve as reliable proxies for identifying the confinement regime and predicting the performance of nanocrystals in target applications. However, apart from performance in potential applications, unambiguously identifying a "true" type-II may present a challenge from a basic physics point of view, as low optical activity and substantial biexciton binding energy may arise from electrons and holes occupying different atomic layers rather than from the spatial separation of electron and hole wavefunction envelopes. Such "mixed" cases further underscore the necessity of going beyond the envelope function approximation when calculating nanocrystals.

We found that the relative spatial distribution of electron and hole states is highly sensitive to the chemical composition (i.e., Zn, Cu, and In content) and the core/shell geometry. These findings are consistent with previous observations in unalloyed systems. Among the studied heterostructures, core/shell nanocrystals with $Zn_{0.5}In_{0.5}S$ small (1–1.6 nm diameter) cores and relatively thick (1.6 nm) ZnS shells are particularly promising candidates for further investigation. These structures exhibit pronounced type-II behavior, characterized by significant spatial separation of electron and hole wavefunctions, strong biexciton binding energies, and a marked reduction in optical dipole moments. These features indicate enhanced charge separation, making them ideal for photovoltaic applications that require suppressed Auger recombination and extended carrier lifetimes. Conversely, nanocrystals with moderate indium ($In_{0.2}$) and variable copper content demonstrate high tunability between the type-I and type-II confinement regimes. Their partial wavefunction separation enables moderate optical activity and exciton binding. This suggests their utility in light-emitting or bioimaging contexts depending also on core thickness. In these contexts, a trade-off between brightness and exciton stability is advantageous. Taken together, these compositional insights provide concrete guidance for targeted synthesis efforts and more refined computational studies focused on optimizing the confinement and emission properties of cadmium-free nanocrystals. By identifying composition-dependent confinement signatures, this work contributes to the rational design of safer, application-optimized quantum dot materials and lays the groundwork for predictive modeling of complex heterostructures beyond the traditional Cd-based systems.

Methods

For the calculation of nanocrystal energy spectra, including HOMO–LUMO gaps, we used the ETB method within the sp^3s^* model[23], with parameters fitted to reproduce key bulk properties such as the band gap. For ZnS, we adopted the parameter set by Lippens et al.[19] which was further extended to include spin–orbit coupling effects following the procedure described in Chadi's research paper[26]. For InS and CuS (and in the absence of suitable parameterizations), we adopted experimental room-temperature band gaps of 2.45 eV and 2.1 eV, respectively[13–16]. This choice was justified by the well-known difficulty in accurately calculating bulk band properties for InS and CuS using methods such as DFT. To determine the tight-binding parameterizations for InS and CuS, we used CdS (again, we adopted the CdS parameter set by Lippens et al.[19] with spin–orbit parameters from Chadi[26]) as a reference and modified its parameters to reproduce the experimental band gap and the corresponding band offsets. This adjustment accounts for differences in band alignment between the semiconductors involved in the calculations. Strain-induced changes in bond lengths were modeled using Harrison's law[18]. Since neither experimental nor theoretical band offset values for InS/ZnS or CuS/ZnS were available in the literature, we indirectly inferred these offsets using empirical results from Konovalov and Makhova[27] and Li et al. [28] in combination with the theoretical results from Li et al.[29] This approach indicated a relatively large VBO of 1.1 eV for InS/ZnS and 0.34 eV for CuS/ZnS. However, more recent research[29] has suggested potentially higher VBOs – up to 1.6 eV for InS/ZnS and 0.75 eV for CuS/ZnS. Given the potential variability in VBO values, we compared the results using different VBOs. We emphasize that the estimation of bulk (both natural and strained) band shifts remains a computationally challenging task, and several approaches exist in the literature, often yielding significantly different values. Therefore, studying the influence of VBOs on QD spectra is an important and independent area of research[22].

In atomistic calculations, nanocrystals are simulated as spherical cuts from an underlying zinc-blende lattice. The radius of truncation is always given in units (or halves) of lattice constants to ensure reproducibility. The cut is made by selecting the center of the coordinate system , or the center of the quantum dot on an anion. Several other choices for the center of the coordinate system are possible, leading to different dot stoichiometries and surface terminations (which can be anion-, cation-, or mixed-terminated, depending on the radius), which may be important for small nanocrystals. However, these issues of stoichiometry and surface termination are beyond the scope of the current work and will be addressed comprehensively in our future work.

To model alloying with random compositional fluctuations, we generated a uniformly distributed random number (between 0 and 1) for each cation site in the core region. Based on this number, a zinc atom was replaced with an indium atom with a given probability. To account for lattice constant mismatches (strain effects), we used the valence force field method described in Keating[30]. For ZnS, the method parameters (related to the elastic constants) were taken from the literature[31]. However, due to the lack of available experimental and theoretical data, we used the force constants from CdS for InS and CuS, while the lattice constants were taken directly from experimental measurements[16]. This approximation is justified by the observation that the force constants for ZnS and CdS are very similar within the valence force field method, with the critical strain-related differences mainly due to variations in bond lengths and lattice constants. Therefore, we assumed a similar behavior for InS and CuS. It is worth noting that CuS is nearly lattice-matched with ZnS (resulting in a minor 0.9% strain), while InS exhibits a substantial mismatch of approximately 16%, which leads to exceptionally large strains in unalloyed systems. This significantly limits the feasibility of synthesizing such nanocrystals without alloying. To minimize strain and optimize atomic geometry, we used the conjugate gradient method, assuming free (open) boundary conditions that allow for surface relaxation (though not reconstruction). Subsequently, we performed ETB calculations on the relaxed atomic structures. To calculate several of the lowest-energy electron and hole states, including the ground states, we used the Arnoldi sparse solver as implemented in ARPACK[32]. To eliminate spurious states arising from dangling bonds, we followed the approach proposed by Lee et al.[33] of introducing an energy shift to surface bonds instead of changing the surface atomic energies. This method has proven effective in simulating dangling bond passivation in a wide range of QD systems. In this work, we applied a shift of 20 eV to each dangling bond to effectively shift spurious surface states far away from the gap region. One possible implementation of this approach involves identifying atoms in the system without all four nearest neighbors, determining the direction of the missing neighbor, and applying a shift to the hybridized orbital associated with that direction. In our simpler approach, we first shift the energies of all orbitals (all four hybrids) and then apply negative shifts to the actual neighbors. This effectively cancels the passivation for the real neighbors, while applying it only to the missing neighbors, i.e., the dangling bonds.

In the virtual crystal approximation (VCA), the tight-binding parameters of an alloyed system are derived by linearly interpolating the bulk parameters of its constituent materials . In this case, we assume a uniform, unstrained, perfect lattice with no strain or randomness due to alloying. When strain is neglected in the calculation (NSTR), we account for alloy randomness or composition mixing. However, strain is still neglected; that is, four identical bond lengths to nearest neighbors and ideal angles between bonds are assumed, as in the perfect tetrahedral lattice. Finally, no such simplifications are made in the calculation that accounts for strain (STR).

Following the tight-binding calculations, excitonic spectra[34] were calculated using the configuration-interaction method described in detail in Zieliński et al.[20] The optical spectra were then obtained by calculating the photoluminescence intensity resulting from the electron–hole pair recombination using Fermi's golden rule. Many-body calculations were performed with a minimal basis set, including the two lowest electron states (with spin) and the four highest hole states (with spin), as our goal was to use optical transition rates to approximately characterize the type of confinement. The electron–electron (J_{E1E1}), hole-hole (J_{H1H1}), and electron–hole (J_{E1H1}) integrals used to estimate the biexciton binding energy were calculated using the approach also described in detail in Zieliński et al.[20].

Conclusions

This study demonstrates the power of comprehensive atomistic modeling to advance the understanding of ZnCuInS/ZnS core/shell nanocrystals and guide their rational design. By exploring a wide range of core compositions, shell thicknesses, and geometric configurations, we provide deep insight into the complex interplay between confinement regimes, electronic structure, and optical behavior in cadmium-free nanocrystals. Our findings highlight how subtle variations in material parameters can lead to type-I, type-II, or mixed confinement, each with distinct implications for electron–hole overlap, exciton dynamics, and optical performance. From a practical perspective, these findings provide valuable design principles for tailoring the properties of QDs to meet the needs of emerging technologies. In particular, nanocrystals exhibiting type-II or mixed confinement show strong potential for applications that benefit from enhanced exciton-exciton repulsion. Moreover, the ability to predict and control confinement properties and optical activity at the atomic scale is essential for assessing the environmental and health effects of nanomaterials and nanocrystals, especially as their use in industrial and biomedical applications expands. Finally, this work positions ZnCuInS/ZnS nanocrystals as promising candidates for next-generation applications in photonics and bioimaging. Our integrated approach—combining atomistic modeling with compositional and geometric optimization—establishes a robust framework for designing nanostructures with precisely engineered optoelectronic properties.

Data availability

The datasets used and/or analysed during the current study available from the corresponding author on reasonable request.

Received: 17 May 2025; Accepted: 1 August 2025

References

1. Shirasaki, Y., Supran, G. J., Bawendi, M. G. & Bulović, V. Emergence of colloidal quantum-dot light-emitting technologies. *Nat. Photon.* **7**, 13–23. https://doi.org/10.1038/nphoton.2012.328 (2013).
2. Karatum, H. et al. Cadmium-free and efficient type-II InP/ZnO/ZnS quantum dots and their application for LEDs. *ACS Appl. Mater. Interfaces.* **13**, 12345–12355. https://doi.org/10.1021/acsami.1c08118 (2021).
3. Rogers, K. E., Nag, O. K., Stewart, M. H. & Delehanty, J. B. Recent advances in the use of cadmium-free quantum dots for bioimaging. *Mater. Matters* **16**, 2. https://doi.org/10.1016/j.apmt.2020.100840 (2021).
4. Miao, S. & Cho, Y. Toward green optoelectronics: Environmental-friendly colloidal quantum dots photodetectors. *Front. Energy Res.* **9**, 666534. https://doi.org/10.3389/fenrg.2021.666534 (2021).
5. Zhang, W., Pan, C., Cao, F., Wang, H. & Yang, X. Highly bright and stable white-light-emitting cadmium-free Ag,Mn co-doped Zn–In–S/ZnS quantum dots and their electroluminescence. *J. Mater. Chem. C* **6**, 10233–10240. https://doi.org/10.1039/C8TC03742F (2018).
6. Wang, Y.-K. & Liao, L.-S. Wide-bandgap and heavy-metal-free quantum dots for blue light-emitting diodes. *J. Semicond.* **46**, 041101. https://doi.org/10.1088/1674-4926/24100016 (2025).
7. Xu, S. et al. New generation cadmium-free quantum dots for biophotonics and nanomedicine. *Chem. Rev.* **116**, 12234–12327. https://doi.org/10.1021/acs.chemrev.6b00290 (2016).

8. Rakshit, S., Piatkowski, P., Mora-Sero, I. & Douhal, A. Advances in hybrid quantum dot materials: From fundamentals to applications in optoelectronics. *Adv. Opt. Mater.* **10**, 2102566. https://doi.org/10.1002/adom.202102566 (2022).
9. Won, W.-H. et al. Efficient and stable blue quantum dot light-emitting diodes. *Nature* **575**, 634–638. https://doi.org/10.1038/s41586-019-1771-5 (2019).
10. Hu, H.-L. et al. Surface Halogenation of InP quantum dots with zinc halides for enhanced stability and optoelectronic performance. *Inorg. Chem.* **62**, 2877–2886. https://doi.org/10.1021/acs.inorgchem.2c04308 (2023).
11. Martin, R. M. *Electronic Structure: Basic Theory and Practical Methods* (Cambridge University Press, 2020).
12. Jain, A. et al. Commentary: the materials project—A materials genome approach to accelerating materials innovation. *APL Mater.* **1**, 011002. https://doi.org/10.1063/1.4812323 (2013).
13. Nishimo, T., Taniguchi, K. & Hamakawa, Y. Electroreflectance measurements on indium sulfide grown from indium melt. *Solid State Commun.* **19**, 635–637. https://doi.org/10.1016/0038-1098(76)91092-9 (1976).
14. Shaikh, G. Y. et al. Structural, optical, photoelectrochemical, and electronic properties of the photocathode CuS and the efficient CuS/CdS heterojunction. *ACS Omega* **7**, 30233–30240 (2022).
15. Sheardy, A. T., Arvapalli, D. M. & Wei, J. Novel microwave synthesis of near-metallic copper sulfide nanodiscs with size control: Experimental and DFT studies of charge carrier density. *Nanoscale Adv.* **2**, 1054–1058. https://doi.org/10.1039/D0NA00069H (2020).
16. Kushwaha, P. et al. Physical, optical and nonlinear properties of ins single crystal. *Opt. Mater.* **36**, 616–620. https://doi.org/10.1016/j.optmat.2013.10.046 (2014).
17. Perdew, J. P. & Levy, M. Physical content of the exact Kohn-Sham orbital energies: Band gaps and derivative discontinuities. *Phys. Rev. Lett.* **51**, 1884–1887. https://doi.org/10.1103/PhysRevLett.51.1884 (1983).
18. Harrison, W. A. Tight-binding methods. *Surf. Sci.* **299–300**, 298–310. https://doi.org/10.1016/0039-6028(94)90662-9 (1994).
19. Lippens, P. E. & Lannoo, M. Calculation of the band gap for small CdS and ZnS crystallites. *Phys. Rev. B* **39**, 10935–10942. https://doi.org/10.1103/PhysRevB.39.10935 (1989).
20. Zieliński, M., Korkusiński, M. & Hawrylak, P. Atomistic tight-binding theory of multiexciton complexes in a self-assembled InAs quantum dot. *Phys. Rev. B* **81**, 085301. https://doi.org/10.1103/PhysRevB.81.085301 (2010).
21. Ivanov, S. A. et al. Type-II core/shell CdS/ZnSe nanocrystals: Synthesis, electronic structures, and spectroscopic properties. *J. Am. Chem. Soc.* **129**, 11708–11719 (2007).
22. Zieliński, M. Valence band offset, strain and shape effects on confined states in self-assembled inas/inp and inas/gaas quantum dots. *J. Phys. Condens. Matter* **25**, 465301. https://doi.org/10.1088/0953-8984/25/46/465301 (2013).
23. Chadi, D. J. & Cohen, M. L. Tight-binding calculations of the valence bands of diamond and zincblende crystals. *Phys. Status Solidi* **68**, 405–419. https://doi.org/10.1002/pssb.2220680140 (1975).
24. Mourad, D. et al. Band gap bowing of binary alloys: Experimental results compared to theoretical tight-binding supercell calculations for $Cd_xZn_{1-x}Se$. *Phys. Rev. B* **82**, 165204. https://doi.org/10.1103/PhysRevB.82.165204 (2010).
25. Zieliński, M. Influence of substrate orientation on exciton fine structure splitting of InAs/InP nanowire quantum dots. *Nanoscale Res. Lett.* **7**, 265. https://doi.org/10.1186/1556-276X-7-265 (2012).
26. Chadi, D. J. Spin-orbit splitting in crystalline and compositionally disordered semiconductors. *Phys. Rev. B* **16**, 790–796. https://doi.org/10.1103/PhysRevB.16.790 (1977).
27. Konovalov, I. & Makhova, L. Valence band offset at interfaces between CuI and indium sulfides. *J. Appl. Phys.* **103**, 103702. https://doi.org/10.1063/1.2921834 (2008).
28. Li, X. et al. CdTe thin film solar cells with copper iodide as a back contact buffer layer. *Sol. Energy* **185**, 324–332. https://doi.org/10.1016/j.solener.2019.04.082 (2019).
29. Li, Y.-H. et al. Revised ab initio natural band offsets of all group IV, II-VI, and III-V semiconductors. *Appl. Phys. Lett.* **94**, 212109. https://doi.org/10.1063/1.3143626 (2009).
30. Keating, P. N. Effect of invariance requirements on the elastic strain energy of crystals with application to the diamond structure. *Phys. Rev.* **145**, 637–645. https://doi.org/10.1103/PhysRev.145.637 (1966).
31. Martin, R. M. Elastic properties of ZnS structure semiconductors. *Phys. Rev. B* **1**, 4005–4011. https://doi.org/10.1103/PhysRevB.1.4005 (1970).
32. Lehoucq, R. B., Sorensen, D. C. & Yang, C. *ARPACK users' guide: solution of large-scale eigenvalue problems with implicitly restarted Arnoldi methods* (SIAM, 1998).
33. Lee, S., Oyafuso, F., von Allmen, P. & Klimeck, G. Boundary conditions for the electronic structure of finite-extent embedded semiconductor nanostructures. *Phys. Rev. B* **69**, 045316. https://doi.org/10.1103/PhysRevB.69.045316 (2004).
34. Michler, P. (ed.) *Topics in applied physics* Vol. 90 (Springer, 2003).

Acknowledgements

We thank Dr. Andrzej Kędziorski for the valuable discussions regarding the limits of DFT calculations.

Author contributions

M.Z. performed the calculations and prepared the figures. A.G.-S. supervised and acquired funding for the project. Both authors worked on the manuscript.

Funding

The research for this work has received funding from the European Union's Horizon 2020 Research and Innovation Programme under grant agreement no. 953183 (HARMLESS).

Declarations

Competing interests

The authors declare no competing interests.

Additional information

Correspondence and requests for materials should be addressed to M.Z. or A.G.-S.